Defect controlled spin state transitions in FePc adsorbed CrI$_3$

Shamik Chakraborty [b], Guido Fratesi [a,c], Abhilash Ravikumar [b,*]

[a] *Dipartimento di Fisica, Università degli Studi di Milano, Via Celoria 16, Milano 20133, Italy*
[b] *Nanoelectronics Research Laboratory, Department of Electronics and Communication Engineering, Amrita School of Engineering, Amrita Vishwa Vidyapeetham, Bengaluru, India*
[c] *INFN, Sezione di Milano, I-20133 Milano, Italy*

ARTICLE INFO

ABSTRACT

Our study employs first principles to explore the impact of spin on iron phthalocyanine (molecule) upon adsorption onto defect-functionalized CrI$_3$. We focus on three stable vacancy defects commonly found in CrI$_3$, created by the removal of '-Cr-', '-I-' and '-CrI$_3$-' units from the pristine CrI$_3$ lattice, analyzing their electronic and magnetic characteristics in both FM and AFM scenarios. Notably, these defects predominantly affect the electronic structure near the Fermi level. The adsorption of FePc, on defect-functionalized CrI$_3$, exhibits reduced stability compared to the pristine substrate. FePc demonstrates two stable spin states, a 2 μ_B low spin state and a 4 μ_B high spin state. We present two spin-control mechanisms when FePc adsorbs onto these defect-functionalized substrates. We name these — substrate-induced and molecular spin vector-induced control. The former involves manipulating the magnetic order of the substrate (FM/AFM), leading to molecular spin state transitions. The latter mechanism involves modifying the spin orientation on the molecular Fe atom relative to the substrate's spin (parallel/antiparallel), resulting in molecular spin state transitions. This research proposes novel effective methods to control the spin states of magnetic metal complexes during adsorption onto magnetic substrates, offering potential applications in molecular electronics and spintronics.

1. Introduction

Molecular spintronics and its potential applications can be realized using molecular semiconductors [1] which have long relaxation time and weak spin–orbit coupling [2]. Molecular semiconductors, known for their spinterface-like mechanical flexibility [3], photovoltaic characteristics [4], ferroelectric properties [5], and interfacial interactions based on magnetic exchange [6], present a promising avenue for applications in the field of molecular spintronics. This emerging field, at the forefront of miniaturization [7–9], combines molecular electronics with single-molecule magnets [10], offering diverse functionalities such as magnetoresistance (MR) effect [11–13], spin-filtering effect [14, 15], spin rectification effect [16,17], Kondo effect [18,19], and spin caloritronics [20,21], which exploit the utilization and manipulation of electron spin in organic molecular materials. The rise of multifunction molecular spintronic devices and their potential applications such as spin organic LEDs [3], molecular photovoltaic devices [22] can be achieved by combining the opto-electrical properties of molecules with spin valves. The modulation and control of spin states in molecular complexes adsorbed on substrates are essential for the design of nanoscale spintronic devices, as exemplified by the remarkable spin transport properties observed in transition metal phthalocyanine

(TMPc) molecules, including significant magnetoresistance (MR) and spin-filter effects [23–25]. In a study, cobalt and manganese phthalocyanine molecule based magnetic tunnel junctions (MTJs) were examined, revealing that CoPc MTJs demonstrate significant tunneling magnetoresistance (TMR) and tunneling anisotropic magnetoresistance (TAMR) effects, whereas MnPc MTJs exhibit a remarkable giant TAMR effect reaching ratios up to ten thousand percent [26]. Iron Phthalocyanine (FePc) junction exhibits high spin-filter efficiency and negative differential resistance (NDR) across various edge shapes and widths of graphene nanoribbons (GNRs) and N-doping sites, suggesting its potential for molecular electronics and spintronics applications [27]. TMPc-based molecular junctions with borophene nanoribbon electrodes exhibit high magnetoresistance (MR) ratios, reaching 303% and 368% for MnPc and FePc junctions [13], respectively, while also demonstrating almost perfect spin-filter efficiency (SFE) at low temperatures, making them promising candidates for future molecular spintronic devices [10,28].

FePc, known for its desirable properties in studying magneto-optical and electrical effects, as well as quantum ferromagnetism, has been extensively investigated [29–31]. The magnetic moment of the free-standing FePc molecule is primarily localized around the Fe atom,

---

* Corresponding author.
E-mail address: r_abhilash@blr.amrita.edu (A. Ravikumar).

with a calculated value of 2 μ_B [32,33]. The adsorption of H_2 and H_2O molecules on FePc maintains the magnetic moment at 2 μ_B [32]. Adsorbing O_2, CO, and N_2 molecules on FePc results in a reduction of the magnetic moments to 0 μ_B [32]. This is attributed to the antiferromagnetic coupling between the O_2 molecule and the Fe atom, while the strong interaction of CO and N_2 molecules causes a shift of the dz^2 orbital to a higher level and a cancellation of the spin magnetic moments due to the low spin configuration [32]. At the atomic monolayer scale, molecular oxygen intercalation between the FePc molecule and the surface leads to a significant increase in the Fe magnetic moment, transforming it from nearly negligible to an order of magnitude larger value, thus demonstrating the reversible bifunctional chemical-magnetic switch property of FePc [34]. Conventional magnetic measurements and advanced techniques such as x-ray magnetic circular dichroism [35] reveal a strong correlation between the magnetic behavior of MPc molecules and the hybridization of the electronic ground state of the central metal atom with ligand states (intra-molecular interaction), while in bulk and thin films with stacked molecules, the magnetic properties are governed by intermolecular exchange interactions between magnetic M atoms [36].

The fabrication of FePc thin films on substrates allows for control over ferromagnetism and molecular orientation, presenting new opportunities for flexible spintronic devices [37]. The adsorption of FePc on Co[001], specifically in the on-top-of Co position rotated by 45° relative to the substrate orientation, strongly affects the magnetic coupling while maintaining the unaltered spin state of S = 1 [38]. When FePc is placed on Ag(111), there is a transfer of charge between the molecule and the substrate, involving the 3d-open shell. However, when FePc is placed on Au(100), there are no significant changes in the electronic situation between the molecule and the substrate [39]. Removal of the outermost H atoms in FePc diminishes the Fe–Au coupling and triggers a transition from a Kondo state to a magnetic triplet state [40]. Hybrid systems combining graphene and FePc exhibit high magnetic anisotropic energy, making them promising candidates for graphene-single magnetic molecule (SMM) systems [41]. Physisorption of FePc molecules on graphene and MoS_2 induces large spin dipole moments, leading to a significant reduction in the effective magnetic moment as observed in XMCD experiments [42]. The introduction of vacancy defects in graphene alters the spin state of FePc from S = 1 to S = 2 in graphene/FePc heterostructures [43]. Spin state tunability of FePc can also be achieved through coordination with surplus hydrogen atoms [43]. The individual distribution of transition metal (TM) atoms, especially in the 2D magnetic materials CrI_3, $Cr_2Ge_2Te_6$, and Fe_3GeTe_2, could potentially be achieved by incorporating iron atoms into the 2D phthalocyanine (Pc) sheet of the FePc system.

The magnetic behavior of 2D magnet CrI_3 is influenced by the number of layers and interlayer stacking arrangements, with interlayer magnetic interactions and the underlying cause of magnetic ordering explained through orbital analysis [44]. Distinct spatial distributions of localized defect states were observed and characterized using high-resolution scanning tunneling microscopy (STM) for the three primary intrinsic point defects in CrI_3: iodine vacancy (VI), chromium vacancy (VCr), and multiatom CrI_3 vacancy (VCrI$_3$) [45]. The magnetic moments in CrI_3 are influenced by these stable point defects, leading to ferromagnetic (FM)-antiferromagnetic (AFM) phase transitions [46]. In a recent investigation of charged defects in monolayer CrI_3, positively charged I vacancies and negatively charged Cr vacancies, atom relaxation causes a blue and red-shift of defect states near the Fermi level [47]. Oxygen defect functionalization of CrI_3 reduces the bandgap by 58% while preserving its magnetic properties at higher Curie temperatures [48]. In bilayer CrI_3, doping and interlayer atomic intercalation induce an antiferromagnetic to ferromagnetic phase transition through exchanged superexchange interactions between Cr atoms in the interlayer [49]. Furthermore, the adsorption of benzene molecules on CrI_3 enhances its optical absorption and ferromagnetic coupling [50]. With the motivation to explore the behavior of adsorbed 2D magnetic molecules like FePc on defect functionalized 2D magnetic substrate CrI_3, we aim to explore their potential for realizing spintronic-based applications.

In this study, we investigate the electronic structure of FePc adsorbed on defect-functionalized CrI_3 and demonstrate the controllable spin state of Fe can be achieved through two mechanisms: substrate-induced spin control and molecular vector-induced spin control. We describe the computational methods employed and present the optimized geometrical configurations of FePc adsorbed on defect-functionalized CrI_3. The electronic structure of FePc/*def*-CrI_3 is discussed, considering the effects of substrate spin configuration switching and spin vector orientation.

2. Computational details

We perform *ab-initio* density functional theory (DFT) calculations [51] within the Quantum Espresso platform [52]. We use Perdew–Burke–Ernzerhof (PBE) exchange correlation functional [53] with generalized gradient approximation (GGA), a plane wave basis set and an ultrasoft scalar relativistic pseudopotential for the calculations [54]. The Hubbard parameter [55] for Fe and Cr atoms are set to U_{eff} = 5 eV [56] and 3 eV [57] respectively, to take into account the on-site Coulombic interactions of their extended *d* orbitals. The kinetic energy cut off is set to 48 Ry and charge density cut off is set to 460 Ry. We construct a supercell of FePc adsorbed on $\sqrt{7} \times \sqrt{7}$ CrI_3 with a minimum inter-molecular separation of ~3 Å to avoid directional lateral interactions (known to cause characteristics development at high coverage) [58], and a vacuum separation of 15 Å (to minimize interactions between periodic images [49]). The interlayer interactions for the heterostructures are addressed by considering a van der Waals Grimme D-2 correction [59]. We perform fixed cell relaxation until the minimum Hellmann–Feynman force [60] on all atoms is lesser than 10^{-3} eVÅ^{-1}. A Γ point Monkhorst pack [61] k-mesh is used to sample the Brillouin zone [62] for the electronic structure relaxations. To examine the electronic and magnetic properties of FePc on functionalized CrI_3, the spin dependent molecular projected density of states is visualized with a $3 \times 3 \times 1$ Γ centered k-grid, with a Gaussian smearing of 3 mRy. The electronic charge transfer between the layers is quantified by atomic orbital-based Löwdin parameterization [63].

3. Results and discussion

3.1. Configurations of FePc/defect-functionalized CrI$_3$

Fig. 1 (a–d) shows the various stable configurations of (a) pristine $\sqrt{7} \times \sqrt{7}$ CrI_3 and (b-d) defect functionalized CrI_3. The lattice parameter of primitive CrI_3 is 7.008 Å [54] and correspondingly for $\sqrt{7} \times \sqrt{7}$ CrI_3 is 18.35 Å. The reason we consider a $\sqrt{7} \times \sqrt{7}$ CrI_3 is that upon adsorption of FePc, a minimum inter-molecular separation of ~3 Å is necessary to describe sufficiently diluted molecules [64]. For anti-ferromagnetic configurations, the spin-up and spin-down magnetic moments on 'Cr' atoms are represented by 'light blue' and 'dark blue' shades respectively.

In order to functionalize pristine $\sqrt{7} \times \sqrt{7}$ CrI_3, we consider two point defects and one crystal vacancy defect, each neutrally charged as shown in Fig. 1 (b–d) respectively. The three vacancy defects considered are the most stable charge-neutral defective configurations observed in CrI_3 with VI being the most stable defect among them [46]. In Fig. 1(b), a central Cr atom is removed (shown by red dashed circles) and the defect states considered are contributed by its nearest neighbor atoms (shown by green solid circles). This geometrical configuration is named as VCr-CrI_3 and the number of I atoms (with defect states) available in the structure is 6. In Fig. 1(c), we create an 'I' point defect and the corresponding defect states are contributed by the nearest neighbor Cr atoms (termed as Cr(D*)) and the I atoms (termed as I(D*)) of the I-Cr-I bond pair [65,66]. Total number of atoms (with defect
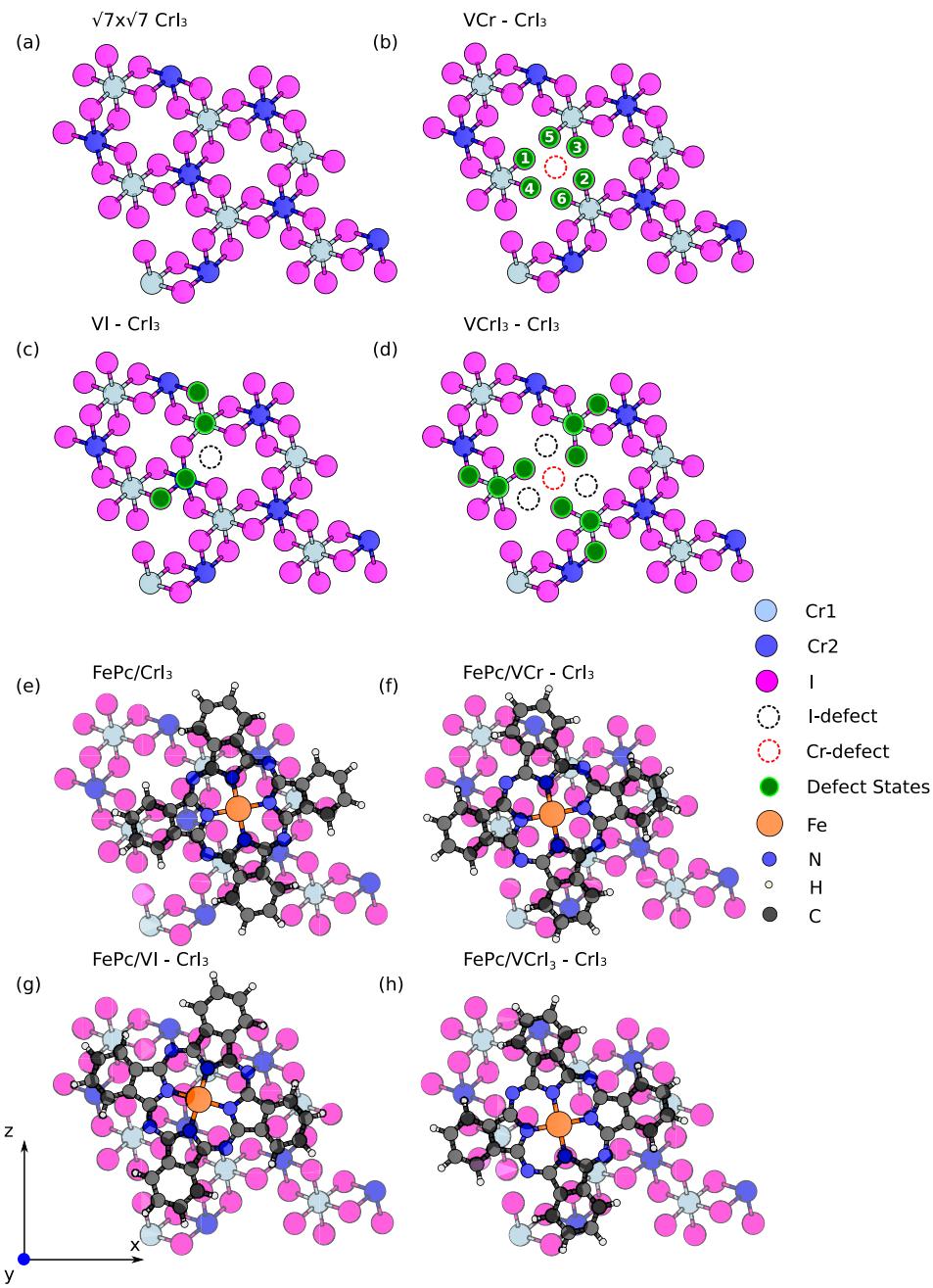
Fig. 1. The crystal structure of (a) pristine $\sqrt{7} \times \sqrt{7}$ CrI_3 (b) CrI_3 with 'Cr' Vacancy (VCr-CrI₃) (c) CrI_3 with 'I' Vacancy (VI-CrI₃) and (d) CrI_3 with 'CrI₃' Vacancy (VCrI₃-CrI₃). The red and black dotted circles represent the absence of Cr and I atoms respectively and the solid green circles represent the neighboring atoms that contribute to the defect states. The light blue 'Cr' atom represents the spin-up states and dark blue 'Cr' atoms the spin-down states. The representation of stable adsorption configurations of (e) FePc/CrI₃ (f) FePc/VCr-CrI₃ (g) FePc/VI-CrI₃ (h) FePc/VCrI₃-CrI₃ after considering translational and rotational symmetry of the system. (For interpretation of the references to color in this figure legend, the reader is referred to the web version of this article.)

states) considered for VI-CrI₃ are 2 Cr atoms and 2 I atoms. For VCrI₃-CrI₃ vacancy, we consider the absence of a CrI₃ sub-group and the nearest neighbor Cr atoms (3 atoms) and the corresponding I atoms of the I-Cr-I pairs (6 atoms) possess defect states as depicted in Fig. 1(d).

To determine the stable adsorption configurations of FePc on functionalized CrI₃, we explore the energy landscape of the substrate taking into account both translational and rotational symmetries of the molecule and calculating the system adsorption energy (E_{ads}) as: E_{FePc/CrI_3}-($E_{FePc} + E_{CrI_3}$) Here E_{FePc/CrI_3} is the total energy of the heterostructure, and E_{FePc}, E_{CrI_3} are the total energy values of gas phase FePc and pristine (or defective) monolayer CrI₃ respectively. The E_{ads} values for the systems in the present study are calculated considering the spin state configuration of the substrate as FM and

parallel spin on Fe for the molecule. The most stable configuration of FePc adsorbed on pristine CrI₃ (as shown in Fig. 1(e)), is when the Fe atom of the molecule is at the center of hollow formed by the 'I' ring. The adsorption energy for FePc/CrI₃ is −1.93 eV and the average molecule–substrate distance is 3.44 Å.

When FePc is adsorbed on VCr-CrI₃ as shown in Fig. 1(f), the most stable morphology is when the Fe atom is on top of the 'Cr' vacancy site (where Cr atom is removed as shown in Fig. 1(b)) with an adsorption energy of −1.77 eV and average interlayer separation of 3.48 Å. FePc is adsorbed on the bridge vacancy site of VI-CrI₃ (where I atom is removed as shown in Fig. 1(c)), as shown in Fig. 1(g) is found to be the most stable configuration with an adsorption energy of −1.82 eV and an optimized interlayer distance is 3.48 Å. In Fig. 1(h), FePc is

Table 1
Summary of adsorption energy (E_{ads}) values for the four primary FePc/*def*-CrI$_3$ configurations.

System name	Adsorption energy E_{ads} (eV)	Interlayer distance (Å)
FePc/CrI$_3$ (Hollow)	−1.93	3.44
FePc/VCr-CrI$_3$ (Top)	−1.77	3.48
FePc/VI-CrI$_3$ (Bridge)	−1.82	3.48
FePc/VCrI$_3$-CrI$_3$ (Top)	−1.02	3.44

adsorbed on the top vacancy site of VCrI$_3$-CrI$_3$ (defect site shown in Fig. 1(d)) with an adsorption energy of the system as −1.02 eV and interlayer distance of 3.44 Å. The details of the adsorption energy for all the possible geometrical configurations of FePc/CrI$_3$ and FePc/*def*-CrI$_3$ (*def*: VCr, VI, VCrI$_3$) are tabulated in Table 1 of Supplementary Information (SI). Summarizing the E_{ads} values presented in Table 1, we find that the pristine FePc/CrI$_3$ configuration is the most stable structure. In the absence of defects, the molecule prefers to occupy the hollow site within the pristine configuration.

3.2. Electronic structure of defect-functionalized CrI$_3$

We now describe the electronic structure of pristine and defect functionalized CrI$_3$ for ferromagnetic (FM) and anti-ferromagnetic (AFM) spin configurations. In Fig. 2(a) the density of states (DOS) of pristine $\sqrt{7} \times \sqrt{7}$ CrI$_3$ is shown for the ferromagnetic case. The bandgap (E_g) obtained for the spin-up channel is ∼0.78 eV [67] where it behaves like a ferromagnetic semiconductor, whereas for the spin-down channel it is ∼3.17 eV, behaving as an insulator [54,68]. The total magnetic moment of the pristine CrI$_3$ is 42 μ_B with the magnetic moment of ∼ 3.45μ_B/atom localized on Cr and ∼ 0.17μ_B/atom on I. For the anti-ferromagnetic $\sqrt{7} \times \sqrt{7}$ CrI$_3$ as shown in Fig. 2 (b), the system is non-magnetic [66] with a bandgap of 0.91 eV in both the spin channels. It is found that the ferromagnetic spin configuration of pristine CrI$_3$ is more stable by ∼600 meV/unit cell compared to its anti-ferromagnetic counterpart [66]. Experimental evidence shows that it is possible to switch the magnetic configurations (FM,AFM) of CrI$_3$ by controlling its growth and aligning its stacking pattern [44].

We now discuss the density of states (DOS) for defect functionalized CrI$_3$ for FM and AFM spin configurations. In Fig. 2(c), the DOS of CrI$_3$ with 'Cr' vacancy defect is shown. The system behaves as a ferromagnetic half-metal (with a total magnetic moment of 36 μ_B [46]) exhibiting metallicity in the spin-up channel and behaves as an insulator with a bandgap of 3.16 eV in the spin-down channel. The DOS projected onto the atoms highlighting defect states reveals that the spin-up states near the Fermi level are predominantly influenced by these defects as shown in the inset of Fig. 2(c). Creating the 'Cr' vacancy changes the magnetic moments of the 'I' defect states from −0.16 μ_B (in the pristine case) to −0.3 μ_B equally localized on all 'I' defect states.

In case of anti-ferromagnetic VCr-CrI$_3$, a Cr spin up atom is removed. The AFM case, VCr-CrI$_3$ behaves as a metal for both spin-up and down channels as represented by the DOS shown in Fig. 2(d). The states at the Fermi level are primarily constituted by 'I' defect states and the total magnetic moment for the AFM case is ∼ 2.1μ_B. The geometry of CrI$_3$ shows three I atoms in a plane above the central 'Cr' (marked as 1,2,3 in Fig. 1(a)), and the remaining in a plane below (marked as 4,5,6 in Fig. 1(a)), and each 'I', one from I-Cr-I bond pair. We find that the magnetic moments of the lower plane 'I-defect' atoms are −0.26 μ_B and that of higher plane 'I-defect' atoms are −0.06 μ_B, both significantly

different from the non-defect I atoms which has a magnetic moment of −0.0002 μ_B. We attribute this to the interfacial magnetic proximity effect [69]. However, the FM state of VCr-CrI$_3$ is energetically more stable by a magnitude of ∼565 meV than its AFM counterpart and consistent with the pristine case.

Fig. 2(e) shows the DOS of VI-CrI$_3$ for the ferromagnetic case. Creating an 'I' vacancy results in VI-CrI$_3$ behaving as a semiconductor with a bandgap of ∼0.25 eV in the spin-up channel and in the spin down channel it behaves as an insulator with a bandgap of 3.28 eV. The 2 Cr and 2 I atoms contribute to an occupied lower energy and unoccupied higher energy defect states in the spin up channel around the Fermi level as shown in the inset of Fig. 2(e). The total magnetic moment of VI-CrI$_3$ is 43 μ_B [46]. The magnetic moments on the defect I in the FM case is −0.18 μ_B and the defect Cr atoms is 3.68 μ_B suggesting a negligible change with respect to the other I and Cr atoms which have a magnetic moments of −0.17 μ_B and 3.44 μ_B respectively. This suggests that creating an I vacancy does not significantly destabilize the magnetic anisotropy of the system and the stability of the electronic structure is conserved by the creation of hybridized lower and higher energy defect states at the Fermi level. This is consistent with other observations of metastable defects in CrI$_3$, where the I adatoms exhibit lower formation energies compared to Cr adatoms across the entire range of chemical potential [46].

For the anti-ferromagnetic VI-CrI$_3$ case shown in Fig. 2 (f), the system is non-magnetic and the electronic structure is consistent with that of pristine CrI$_3$ (Fig. 2(b)). This further supports that creating an I vacancy has little effect on the system's electronic and magnetic structure, except for the appearance of defect states at the Fermi level. It is also observed that the FM state is more stable than the AFM state by ∼615 meV.

The DOS of VCrI$_3$-CrI$_3$ is depicted in Fig. 2(g) for the ferromagnetic case and Fig. 2(h) for the anti-ferromagnetic case. The total magnetic moment for the FM case is 39 μ_B [46] and that of AFM is 3 μ_B. The defect states constituted by 3 Cr atoms and 6 I atoms share the lost charges and contribute towards the lower/higher energy states above the Fermi level as shown in the insets of Fig. 2 (g–h). Due to 'Cr' defect the neighboring 3 I atoms (shown in Fig. 1(d)) compensate for the charge loss. This effect has resemblance to the VCr defect (depicted in Fig. 1(b)), albeit with a distinction: only three I atoms are accessible for compensating the charge deficiency, thereby creating an opportunity for the attraction of spin-down charges. The FM state is more stable by ∼470 meV when compared to the AFM one. The redistribution of magnetic moments across the atoms with defect states displays a composite set of features, blending aspects of both VI and VCr configurations. The Iodine (I) atoms in CrI$_3$ can have different magnetic moments due to the complex interplay between electronic structure, spin–orbit coupling, and the arrangement of neighboring atoms in the crystal lattice. This interaction can lead to a redistribution of spin density, resulting in different magnetic moments for the iodine atoms within the crystal structure of CrI$_3$ [70,71].

We mention that the charge state of the substrate is also influencing the local properties around the defect. For example, charged defects were studied by Ma et al. who found a change up to 0.2 μ_B at Cr atoms around a negatively charged VI, and much smaller (0.01 μ_B) around a positively charged VCr site [47]. We thus believe our conclusions especially for the VCr site (which will exhibit lowest spin transition energies, see below) to hold both in the case of charged and charge-neutral cases. In this manuscript, we focus the discussion on charge-neutral defects.

3.3. Electronic structure of FePc on defect functionalized CrI$_3$

Iron Phthalocyanine (FePc) is a 2-D magnetic metal complex with a planar geometry and is known to retain long-range structural ordering [72] which is found to improve the feasibility of adsorption on crystal surfaces [42]. The stable structure of planar FePc with the
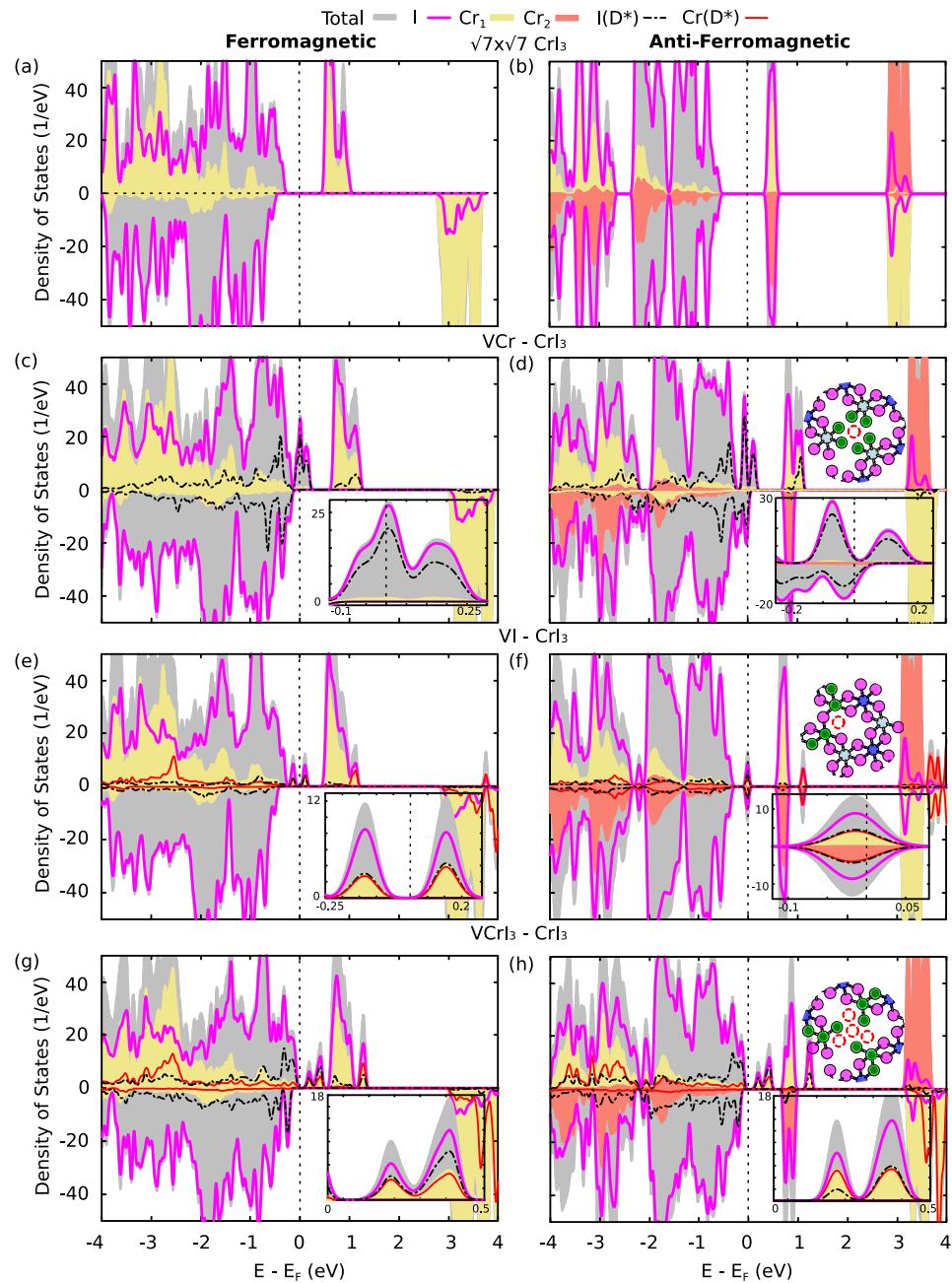
Fig. 2. Spin-resolved density of states (DOS) of ferromagnetic (FM, left panel) and anti-ferromagnetic (AFM, right panel) spin configurations of (a,b) pristine $\sqrt{7} \times \sqrt{7}$ CrI$_3$ (c,d) VCr-CrI$_3$ and (e,f) VI-CrI$_3$ (g,h) VCrI$_3$-CrI$_3$ are visualized with a Gaussian smearing of 0.003 Ry. The insets in (c–h) illustrate the defect states close to the Fermi energy level. The atoms and the corresponding defect states (I - I(D*) an Cr - Cr(D*)) are depicted in the crystal snippets corresponding to each system configuration.

relaxed bond lengths and its electronic structure are shown in the SI. FePc is reported to have two accessible magnetic states - A lower spin state where the magnetic moment on Fe is 2 μ_B [32,73] and a higher spin state of 4 μ_B on Fe atom of FePc [74,75]. Although the lower spin state is considered the stable spin configuration, it is found that the higher spin state is also an energetically accessible magnetic state by ∼300 meV [56,76].

We now discuss the effect of adsorption of FePc on pristine CrI$_3$ for the FM and AFM cases as shown in Fig. 3 (a,b). We can also examine two scenarios: one where the spin orientation on Fe aligns with that of the substrate (parallel case), and another where the spin configuration on Fe is oriented in the opposite direction to that of the substrate (anti-parallel case). It is found that the energy required to flip the spin on Fe from parallel configuration to the anti-parallel one is rather small (∼3 meV) except for cases where magnetic spin transitions are observed

as discussed in the subsequent part of this section. The weak van der Waals interaction of FePc with pristine CrI$_3$ does not significantly alter the electronic configurations of the system as shown in Fig. 3 (a,b). Fe is found to be in its stable low spin state (2 μ_B) for both the cases with the molecular HOMO contributed by the Carbon (C) atoms of FePc close to the Fermi level. For the FM case, the spin-up/spin-down bandgap of the parallel spin configurations are 0.1 eV and 1.06 eV respectively. The bandgap reduces for the AFM case to 0.1 eV in both the spin channels. The adsorption of FePc on pristine CrI$_3$ shows a lack of strong interfacial interaction leading to the electronic charges between the Fe d orbitals to remain uncompensated and FePc retaining a low-spin state as seen in Table 2. From Löwdin analysis, Fe atom shows a net loss of approximately 0.13 electrons. Moreover, the analysis indicates that about 64% of the electronic charge on Fe corresponds to spin-up states,
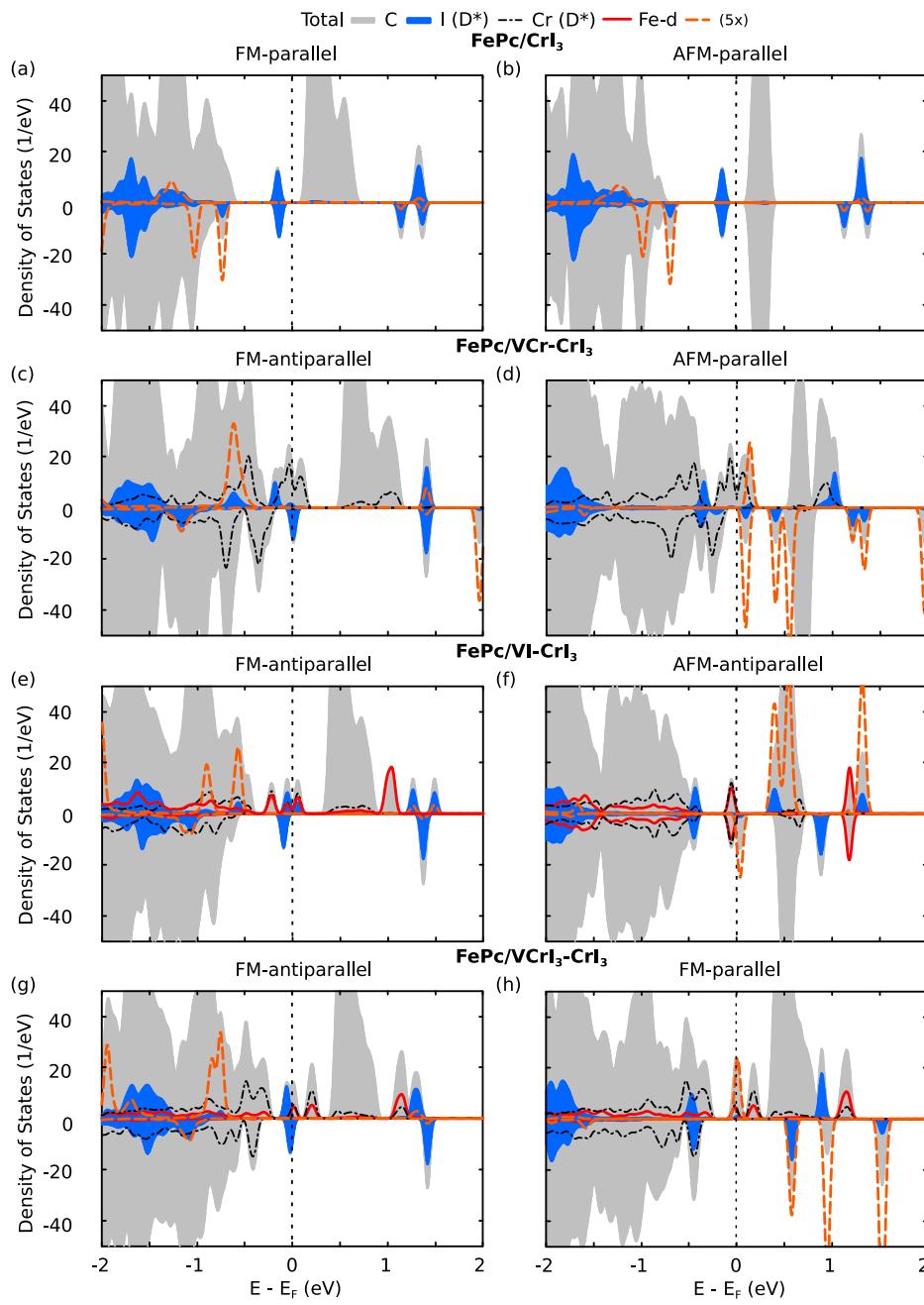
Fig. 3. Spin-resolved DOS for the four systems - (a–b) FePc/CrI$_3$, (c–d) FePc/VCr-CrI$_3$, (e–f) FePc/VI-CrI$_3$, I(D*) and Cr(D*) defect states are magnified by 2.5 times for better visualization and (g–h) FePc/VCrI$_3$-CrI$_3$. The left panel showcases the most energetically stable spin configuration. The subplots (d,f,h) in right panel portrays the spin configuration that leads to the most stable high spin state characterized by Fe - d orbitals interacting with defect states - I(D*) and Cr(D*) at the Fermi energy window.

while approximately 36% corresponds to spin-down states similar to that of gas phase FePc.

The most stable spin configuration for FePc/VCr-CrI$_3$ is when the substrate is ferromagnetic and spin vector on Fe is anti-parallel. The DOS of ferromagnetic FePc/VCr-CrI$_3$ with anti-parallel spin on Fe is shown in Fig. 3(c). The molecular HOMO contributed by Carbon (C) atoms interact with the 'I' defect states. The system is metallic and the absence of substrate states in the spin-down channel pins the molecular HOMO at the Fermi level. Fe loses ~0.13 electrons as shown and exists in the low spin state with a magnetic moment of 2 μ_B, as shown in Table 2. For the AFM case (shown in Fig. 3(d)), when parallel spin FePc is adsorbed on VCr-CrI$_3$, the system is found to relax in the high spin state with the magnetic moment of Fe as $\sim 2.57\mu_B$. The Löwdin population analysis suggests that FePc loses 0.45 electrons which is

70% higher than the ferromagnetic case as shown in Table 2. Fe-d$_{x^2-y^2}$ and Fe-d$_{xy}$ orbitals are found to interact with the defect states of 'I' and Fe relaxes to a high spin state as shown in SI. Due to absence of Cr atom in the substrate, the defect states contributed by (6 I atoms) attract 0.45 electrons lost by Fe. The substrate configuration being AFM permits only spin-down electrons to compensate for the lost electronic charges and contribute to the interfacial interaction. Fe atom is in the parallel spin orientation with 64% spin-up charges and 36% spin-down charges as tabulated in Table 2. Hence, it is easier for Fe to donate electrons in the interaction process. So, we observe in this process Fe loses ~0.45 electrons [77] compared to 0.13 electrons lost when the substrate is FM. This interaction results in Fe with an excess of spin-up charges (~70%) and a diminishing spin-down charges (~30%) as confirmed from Löwdin charges. Therefore in FePc/VCr-CrI$_3$, when the

Table 2

Description of four heterostructure system configurations based on the substrate spin configuration (FM and AFM) with spin orientation (parallel and anti-parallel) on Fe. The different parameters considered are: (i) Löwdin charge analysis showing number of electrons lost(−)/gained(+) by Fe during the interaction (ii) total magnetic moment (μ_B) on Fe and its magnetic state classified as high(**H**)/low(**L**) (iii) Percentage (%) of spin-up (↑ - blue), spin-down (↓ - red) charges available on Fe upon interaction.

System name	FM *parallel*	FM *anti-parallel*	AFM *parallel*	AFM *anti-parallel*
FePc/CrI₃				
Löwdin charge analysis (Fe)	−0.13	−0.13	−0.14	−0.14
μ_B (Fe)	1.75 (**L**)	−1.75 (**L**)	1.75 (**L**)	−1.75 (**L**)
Spin Charge (Fe) (↑ ↓) (%)	64↑ ↓36	36↑ ↓64	64↑ ↓36	36↑ ↓64
FePc/VCr-CrI₃				
Löwdin charge analysis (Fe)	−0.13	−0.13	−0.45	−0.16
μ_B (Fe)	1.84 (**L**)	−1.84 (**L**)	2.57 (**H**)	−1.84 (**L**)
Spin Charge (Fe) (↑ ↓) (%)	64↑ ↓36	36↑ ↓64	70↑ ↓30	36↑ ↓64
FePc/VI-CrI₃				
Löwdin charge analysis (Fe)	−0.12	−0.13	−0.44	−0.46
μ_B (Fe)	1.76 (**L**)	−1.76 (**L**)	2.73 (**H**)	−2.73 (**H**)
Spin Charge (Fe) (↑ ↓) (%)	64↑ ↓36	36↑ ↓64	71↑ ↓29	29↑ ↓71
FePc/VCrI₃-CrI₃				
Löwdin charge analysis (Fe)	−0.61	−0.22	−0.28	−0.28
μ_B (Fe)	2.93 (**H**)	−1.77 (**L**)	1.85 (**L**)	−1.85 (**L**)
Spin Charge (Fe) (↑ ↓) (%)	73↑ ↓27	36↑ ↓64	64↑ ↓36	36↑ ↓64

substrate undergoes magnetic phase transition from FM to AFM, FePc switches from the low spin state to a high spin one when there is a parallel spin orientation on Fe. An alternate spin-control mechanism can be observed where changing the spin vector of FePc from parallel to anti-parallel results in FePc changing its magnetic state from a higher spin state to a lower spin one for the AFM case. 'C' states is pinned to the Fermi level and interacts with the defects in the spin-up channel and exists in the bandgap of CrI₃ in the spin-down one, as shown by the DOS in SI.

It is therefore seen that FePc adsorbed on defect functionalized CrI₃ shows two mechanisms for spin-control: substrate induced spin control and molecular spin vector induced spin control. In substrate induced spin control mechanism, magnetic phase transitions of the substrate from FM to AFM (or AFM to FM) leads to change in the spin state of FePc. Current experimental methods to induce magnetic phase transitions in CrI₃ involve the intrinsic growth of CrI₃ [78] and studies regarding ways to induce magnetic phase transitions in CrI₃ by external factors such as temperature, pressure, external magnetic field, spin–orbit coupling are still ongoing research studies [79–81]. Molecular spin vector induced spin control mechanism is when the change in the molecular spin orientation with respect to the substrate leads to transition in the magnetic states of FePc. This spin manipulation of FePc can be achieved by methods such as photoswitching [82] and pressure induced spin crossover [83].

Adsorption of FePc on VCr-CrI₃ shows both the spin-control mechanisms. For VCr-CrI₃ the difference in energy between FM (parallel) to AFM (parallel) states is 529 meV, which leads to transition of FePc from low spin state to a high spin one. Also, within the AFM substrate, the difference in energy between the parallel and antiparallel spin orientation is 60 meV.

As discussed in the previous section, creating an I vacancy in ferromagnetic CrI₃ leads to an occupied lower energy and unoccupied high energy defect states at the Fermi level in the spin-up channel and a bandgap in the spin-down channel. Adsorption of FePc leads to a weak hybridization of the Carbon (C) HOMO with the defect states in the spin-up channel resulting in a half metal [84,85]. In the spin-down channel, the C states is pinned to the Fermi level and the system shows a bandgap of 1.1 eV as shown in Fig. 3(e). The system is in a low spin state and the magnetic moment of Fe is 1.76 μ_B for the anti-parallel spin orientation. It is observed that FePc/VI-CrI₃ undergoes a substrate induced spin transition where the spin on Fe changes from a low spin state to a high spin one when CrI₃ undergoes a magnetic phase transition from FM to AFM. The characteristics of the high spin state is the interaction of the Fe d orbitals with the substrate states and this can be observed in Fig. 3 (f). The molecular orbital projected density of states (shown in the SI) show the defect states contributed by (Cr and I atoms) interacting with Fe-$d_{x^2-y^2}$ and Fe-d_{xy} orbital states close to E_f for spin down channel and the system switching to a high spin state. From Löwdin population analysis, it is seen that Fe loses 0.44 electrons (~70% more than its FM counterpart) and the magnetic moment on Fe is 2.73 μ_B as tabulated in Table 2. FePc undergoes spin state transition to compensate for the spin-down charges lost by the substrate due to VI defect and achieve magnetic stability. It is validated by spin up charges on Fe, which depletes to 29% compared to 36%, while retaining 71% of spin-down charges compared to 64% (as tabulated in Table 2). The transition of the magnetic spin state of FePc from low to high when adsorbed on VI-CrI₃ is mainly due to substrate induced spin control mechanism. The energy cost required for the magnetic phase transition for VI-CrI₃ from FM to AFM is 850 meV.

When FePc is adsorbed on ferromagnetic VCrI₃-CrI₃ with the Fe spin orientation being anti-parallel to the substrate, exhibits the most stable spin configuration, characterized by a low spin state on Fe. The corresponding DOS is depicted in Fig. 3(g). A spin-vector induced spin transition mechanism is observed by changing the spin orientation of Fe (with respect to the substrate) from anti-parallel to parallel alignment leading to a magnetic state transition of FePc from low spin state to a high spin one as shown in Fig. 3(h) with an energy cost of 446 meV. The system behaves as a ferromagnetic half-metal in the spin up channel and has a bandgap of 0.77 eV in the spin-down channel. The 3 Cr atoms and 6 I atoms (defect states as shown in Fig. 1) interact with Fe-$d_{x^2-y^2}$ and Fe-d_{xy} orbital states as shown in SI. Creating the CrI₃ vacancy depletes the spin-down charges of the substrate to conserve magnetic stability. The adsorption and subsequent interaction of FePc with VCrI₃-CrI₃ leads to Fe donating 0.61 electrons and the spin charge percentage on Fe changing to 73% spin-up charges and 27% spin-down charges from Löwdin population analysis as shown in Table 2. FePc donating the additional spin-down charges to compensate for the defect induced spin-down charge depletion of the substrate leads to FePc stabilizing in a high spin state.

Further, introducing a magnetic phase transition of the substrate from FM to AFM is also found to change the magnetic state of Fe from a high spin state to a low spin one with an energy cost of 289 meV, and the DOS is shown in SI. Adsorption of FePc on anti-ferromagnetic VCrI₃-CrI₃ for either spin orientation of Fe (parallel/anti-parallel) results in a low spin state on FePc. The C states interact with the defect states in the low spin state whereas it was the Fe d orbitals which interacted with the defect states in the most stable high spin state as shown in Fig. 3(h). Therefore FePc adsorbed on VCrI₃-CrI₃ also presents both the spin control mechanisms induced spin state transitions and the total energy cost required for these transitions are of ~446 meV (molecular spin vector induced) and 289 meV (substrate induced).

In Fig. 4(a–f), the spin-resolved DOS for FePc adsorbed on VCr-CrI₃ with a parallel spin vector on Fe is highlighted due to the lower formation energy of the 'VCr' defect [46]. The spin state on Fe remains low (1.84 μ_B) for the FM substrate and transitions to high (2.57 μ_B) in the AFM substrate.
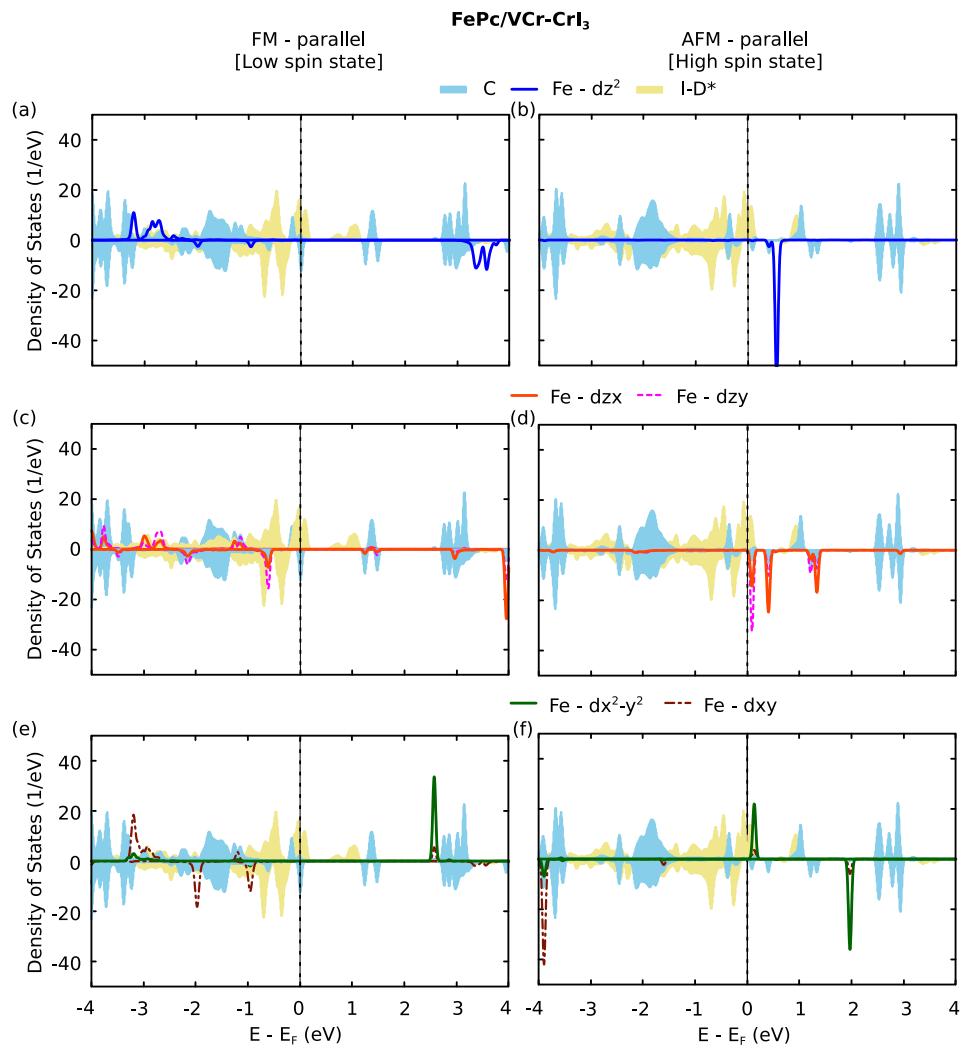
FePc/VCr-CrI₃

Fig. 4. Spin-resolved DOS of FePc/VCr-CrI$_3$ when the spin vector on Fe is parallel to two distinct magnetic orderings of the substrate: (i) FM (left panel) - low spin state on Fe and (ii) AFM (right panel) - high spin state on Fe, projected on C states (FePc) and I(D*) defect states (VCr-CrI$_3$) and on Fe-d suborbitals - (a,b) Fe-d$_{z^2}$ (blue) (c,d) Fe-d$_{zx}$ (orange) and d$_{zy}$ (dashed magenta) (e,f) Fe-d$_{x^2-y^2}$ (green) and d$_{xy}$ (long-dashed red). The Fe-d suborbitals are magnified by a factor of 5 for improved visualization. (For interpretation of the references to color in this figure legend, the reader is referred to the web version of this article.)

The interaction of Fe-d suborbitals with C states and I(D*) states of VCr-CrI$_3$ is shown in Fig. 4(a–f). Notably, Fe-d$_{z^2}$ exhibits negligible interaction with I(D*) states in the FM substrate (Fig. 4(a)) but interacts with C states. In Fig. 4(b), for the AFM substrate, the spin-down charges of Fe-d$_{z^2}$ deplete by 61%, shifting to unoccupied levels with no significant C state interaction.

Fe-d$_{zx}$ and d$_{zy}$ orbitals exhibit electronic states interacting with C states in both spin channels for the FM substrate as depicted in Fig. 4(c). In the AFM substrate, these orbitals do not exist in the spin-up channel, with significant interaction in the spin-down channel, as shown in Fig. 4(d). Spin-down charges deplete by 80% and 77%, shifting to unoccupied levels.

Fig. 4(e,f) shows Fe-d$_{x^2-y^2}$ and d$_{xy}$ orbitals interact with C states for both substrates. In the AFM case (Fig. 4(f)), these orbitals interact with I(D*) defect states, gaining 59% spin-up and 61% spin-down charges, facilitating interaction with the defect states.

To summarize, in the VCr-CrI$_3$ FM case, Fe loses 0.13 electrons (Table 2), maintaining a low spin state characterized by Fe-d suborbital interaction with C states. Switching the magnetic order of the substrate to AFM, results in Fe losing 0.45 electrons (Table 2), with Fe-d$_{z^2}$, d$_{zx}$, d$_{zy}$ suborbitals depleting in spin-down charges, interacting with C states. Fe-d$_{x^2-y^2}$ gains both spin-up and spin-down charges, allowing interaction with I(D*) defect states, facilitating a switch from low to high spin state.

Fig. 5 illustrates graphical representations of spin state transitions, shifting between the low spin state and the high spin state, and vice versa, for FePc adsorbed on pristine and defect-functionalized CrI$_3$. Four specific spin configurations are considered for each system: FM substrate with parallel/antiparallel spin on Fe and AFM substrate with parallel/antiparallel spin on Fe. Notably, for defect-functionalized systems, it becomes possible to access two distinct magnetic states of Fe — the low spin state and the high spin state. These spin state transitions and the ability to attain two different magnetic states within a system are governed by two spin mechanisms: substrate-induced spin control and molecular vector-induced spin control. Substrate-induced spin control occurs when the spin orientation on Fe remains unchanged, but the magnetic order of the substrate switches between FM and AFM, or vice versa. Molecular vector-induced spin control involves changing the spin vector on Fe from parallel to antiparallel within the same magnetic order of the substrate, leading to a state transition.

In Fig. 5(a), FePc adsorbed on CrI$_3$ exhibits the most stable spin configuration with FM parallel alignment. The magnetic order of CrI$_3$ can transition from FM to AFM at an energy cost of 622 meV, but no spin state transition occurs among the four spin configurations.

In Fig. 5(b), upon adsorption of FePc on VCr-CrI$_3$, the most stable spin configuration occurs when the substrate is FM, and the spin on Fe is antiparallel. Here, both types of spin state transitions are observed.
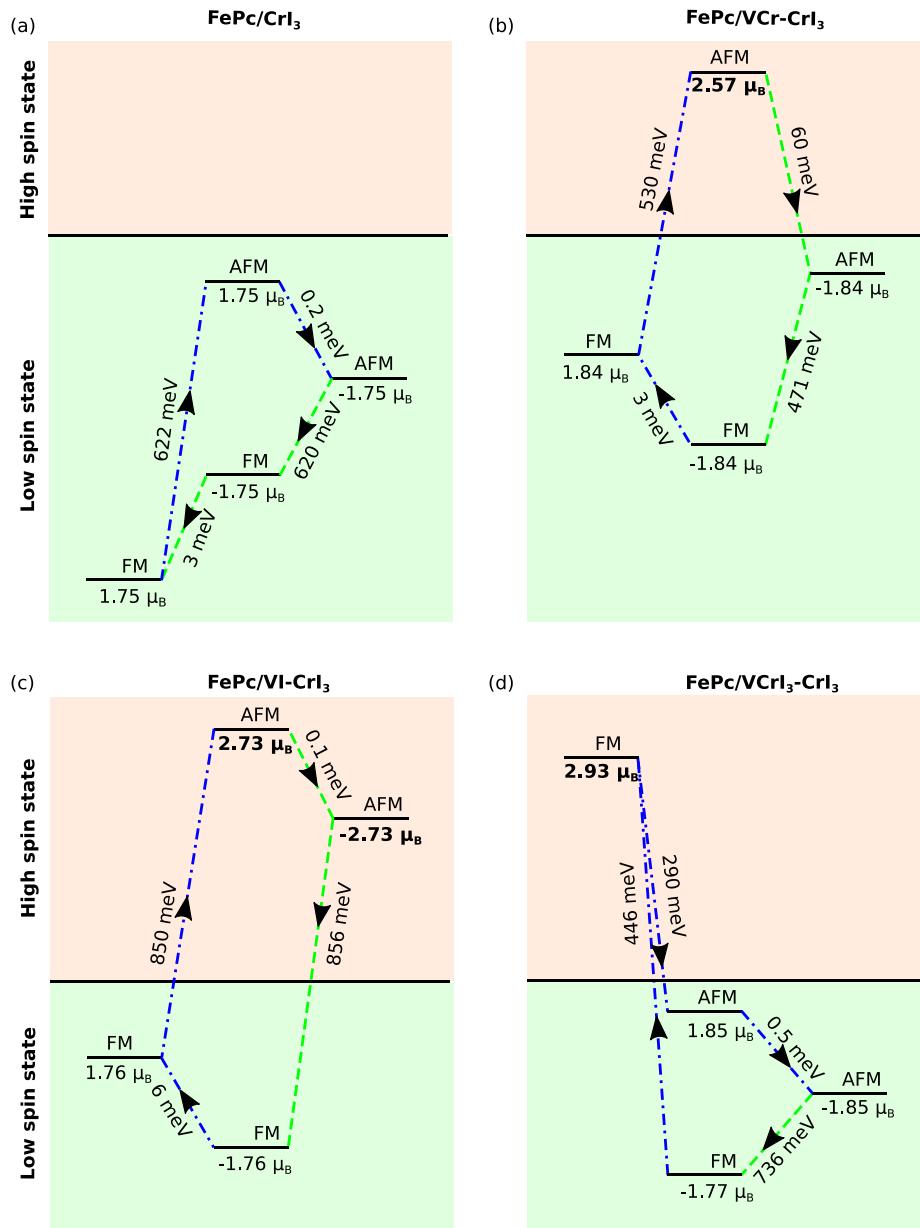
Fig. 5. Schematic representation (not displayed to scale) of possible spin state transitions between spin configurations with spin magnetic moment values (μ_B) for : Ferromagnetic (FM) - Parallel/Antiparallel and Antiferromagnetic (AFM) - Parallel/Antiparallel configurations in systems with FePc adsorbed on (a) CrI_3, (b) VCr-CrI_3, (c) VI-CrI_3, and (d) $VCrI_3$-CrI_3. The transition from the low spin state (indicated by the green shade) to the high spin state (highlighted in a crimson shade) is graphically conveyed through the division of each half by a solid line. The most stable spin configuration for each system is represented in the bottom most half, corresponding to the low spin state. The transition from low to high spin state is depicted in the upper half, indicating the change in spin configuration. For changing each spin configuration, the energy cost (denoted in meV alongside the lines) incurred is represented by blue dash-dotted lines, whereas the energy cost saved is displayed as green dashed lines. (For interpretation of the references to color in this figure legend, the reader is referred to the web version of this article.)

Transitioning the magnetic order of the substrate from FM to AFM results in a spin state transition from low to high, incurring an energy cost of 530 meV. This state is less stable than the FM substrate spin configuration. In the AFM magnetic order, the spin state on Fe shifts from high to low only by changing the spin on Fe from parallel to antiparallel. Additionally, the AFM antiparallel spin configuration is energetically more favorable than its parallel counterpart by an order of 60 meV.

Fig. 5(c) presents the spin state transition for FePc adsorbed on VI-CrI_3, focusing on the substrate spin control mechanism. The spin state on Fe transitions from low to high by changing the magnetic order of the substrate from FM to AFM, incurring an energy cost of approximately 850 meV. It remains in the same spin state when altering the spin vector from parallel to antiparallel. The state transitions from

high to low when the magnetic order changes from AFM to FM, with an unchanged antiparallel spin configuration on Fe. This state transition is more stable, and the energy cost reduces proportionately to approximately 850 meV.

Finally, in Fig. 5(d), the spin state transition for FePc adsorbed on $VCrI_3$-CrI_3 is depicted. In this case, the most stable spin configuration is FM antiparallel. The transition from high to low spin state is achieved by utilizing both spin control mechanisms. When the spin configuration is FM antiparallel, it is in the low spin state. Changing the spin on Fe from parallel to antiparallel results in a transition to the low spin state, incurring an energy cost of 446 meV. To switch back from the high to low spin state, the magnetic order of the substrate can be changed from FM to AFM, with an energy expenditure of approximately 300 meV.

Most of the energy costs we compute for the low-spin to high-spin transitions are of the order of few hundreds of meV, therefore much higher than values typically encountered in spin crossover systems [86], we remark the reduction by about one order of magnitude in the case of FePc/VCr-CrI$_3$ (60 meV). This, while still being reasonably too high for practical use by immediate experiments, suggests further work on this topic for example on other possible hybrid molecule/substrate systems. Possibly, this approach could be combined with others being considered, for example with chemical-induced spin transitions as observed for FePc/Cu(100) with XMCD experiments by NO$_2$ exposure [87].

4. Conclusion

In this study, we investigate the spin-dependent electronic structures of FePc (molecule) adsorbed on defect-functionalized CrI$_3$. We consider three most stable vacancy defects observed in CrI$_3$, created by removing 'Cr', 'I' and CrI$_3$ units from the pristine 'CrI$_3$' lattice and study their electronic and magnetic properties in both FM and AFM cases. The defect states are predominantly found at the Fermi level altering the electronic structure of the systems. FePc when adsorbed on defect functionalized CrI$_3$ shows lower stability when compared to the pristine substrate and its interaction with defective CrI$_3$ modifies its magnetic properties (for example the energy cost for the FM-AFM transition reduces from 0.62 eV in antiparallel FePc/CrI$_3$ to 0.47 eV in FePc/VCr-CrI$_3$). FePc exhibits two stable spin states of 2 μ_B (low spin state) and 4 μ_B (high spin state) and we present two mechanisms of spin-control when FePc is adsorbed on defect functionalized CrI$_3$. The first one, that we name substrate induced spin control involves changing the magnetic order of the substrate (FM/AFM) which leads to molecular spin state transitions as observed in FePc/VCr-CrI$_3$, FePc/VI-CrI$_3$ and FePc/VCrI$_3$-CrI$_3$. In molecular spin vector induced spin control, changing the spin orientation on Fe (of FePc) with respect to the spin of the substrate (parallel/antiparallel) results in the molecular spin state transitions as observed for FePc/VCr-CrI$_3$ and FePc/VCrI$_3$-CrI$_3$. While the energies we compute are still outside practical use by immediate experiments, the significant reduction of energy costs (nearly one order of magnitude) that we obtain for FePc/VCr-CrI$_3$ appear promising, also considering that up to our knowledge no such dramatic reduction was reported on another magnetic substrate. This work therefore highlights potential mechanisms to control the spin states of magnetic metal complexes when adsorbed on magnetic substrates for candidate applications in molecular electronics and spintronics.

CRediT authorship contribution statement

Shamik Chakraborty: Writing – review & editing, Writing – original draft, Visualization, Validation, Software, Methodology, Investigation, Formal analysis, Data curation, Conceptualization. **Guido Fratesi:** Writing – review & editing, Writing – original draft, Visualization, Validation, Supervision, Software, Resources, Methodology, Investigation, Funding acquisition, Formal analysis, Conceptualization. **Abhilash Ravikumar:** Writing – review & editing, Writing – original draft, Visualization, Validation, Supervision, Software, Resources, Project administration, Methodology, Investigation, Funding acquisition, Formal analysis, Data curation, Conceptualization.

Declaration of competing interest

The authors declare that they have no known competing financial interests or personal relationships that could have appeared to influence the work reported in this paper.

Data availability

No data was used for the research described in the article.

Appendix A. Supplementary data

Supplementary material related to this article can be found online at https://doi.org/10.1016/j.surfin.2024.104452.

References

[1] Guillaume Schweicher, Guillaume Garbay, Rémy Jouclas, François Vibert, Félix Devaux, Yves H. Geerts, Molecular semiconductors for logic operations: Dead-end or bright future? Adv. Mater. 32 (10) (2020) 1905909.

[2] Christoph Boehme, John M. Lupton, Challenges for organic spintronics, Nat. Nanotechnol. 8 (9) (2013) 612–615.

[3] Xiangnan Sun, Amilcar Bedoya-Pinto, Roger Llopis, Fèlix Casanova, Luis E. Hueso, Flexible semi-transparent organic spin valve based on bathocuproine, Appl. Phys. Lett. 105 (8) (2014).

[4] Tho D. Nguyen, Eitan Ehrenfreund, Z. Valy Vardeny, Spin-polarized light-emitting diode based on an organic bipolar spin valve, Science 337 (6091) (2012) 204–209.

[5] Dali Sun, Mei Fang, Xiaoshan Xu, Lu Jiang, Hangwen Guo, Yanmei Wang, Wenting Yang, Lifeng Yin, Paul C. Snijders, T.Z. Ward, Zheng Gai, X.-G. Zhang, Ho Nyung Lee, Jian Shen, Active control of magnetoresistance of organic spin valves using ferroelectricity, Nature Commun. 5 (4396) (2014) 1–6.

[6] Karthik V. Raman, Alexander M. Kamerbeek, Arup Mukherjee, Nicolae Atodiresei, Tamal K. Sen, Predrag Lazić, Vasile Caciuc, Reent Michel, Dietmar Stalke, Swadhin K. Mandal, Stefan Blügel, Markus Münzenberg, Jagadeesh S. Moodera, Interface-engineered templates for molecular spin memory devices, Nature 493 (7433) (2013) 509–513.

[7] Alexandre R. Rocha, Víctor M. García-suárez, Steve W. Bailey, Colin J. Lambert, Jaime Ferrer, Stefano Sanvito, Towards molecular spintronics, Nature Mater. 4 (2005) 335–339.

[8] Lapo Bogani, Wolfgang Wernsdorfer, Molecular spintronics using single-molecule magnets, Nature Mater. 7 (3) (2008) 179–186.

[9] Stefano Sanvito, Molecular spintronics, Chem. Soc. Rev. 40 (6) (2011) 3336–3355.

[10] Juan Yang, Xuesong Liang, Zhizhou Yu, Magnetoresistance and spin-dependent Seebeck effects in phthalocyanine-based molecular junctions with borophene electrodes, Physica E 151 (2023) 115731.

[11] Derek Waldron, Paul Haney, Brian Larade, Allan MacDonald, Hong Guo, Non-linear spin current and magnetoresistance of molecular tunnel junctions, Phys. Rev. Lett. 96 (16) (2006) 166804.

[12] Stefan Schmaus, Alexei Bagrets, Yasmine Nahas, Toyo K. Yamada, Annika Bork, Martin Bowen, Eric Beaurepaire, Ferdinand Evers, Wulf Wulfhekel, Giant magnetoresistance through a single molecule, Nat. Nanotechnol. 6 (2011) 185–189.

[13] L.L. Tao, J. Wang, Giant magnetoresistance and perfect spin filter effects in manganese phthalocyanine based molecular junctions, Nanoscale 9 (34) (2017) 12684–12689.

[14] L. Zhu, K.L. Yao, Z.L. Liu, Molecular spin valve and spin filter composed of single-molecule magnets, Appl. Phys. Lett. 96 (8) (2010).

[15] Yingjie Jiang, Yadong Wei, Yuxiu Wang, Kaner Tolbert Ngeywo, Yangyang Hu, Songsong Wang, Kaijuan Pang, Guiling Zhang, Weiqi Li, Yongyuan Jiang, Perfect spin filtering in homobimetallic Ni complex with high tolerance to structural changes, J. Phys. Chem. Lett. 10 (24) (2019) 7842–7849.

[16] C. Zhou, M.R. Deshpande, M.A. Reed, L. Jones Ii, J.M. Tour, Nanoscale metal/self-assembled monolayer/metal heterostructures, Appl. Phys. Lett. 71 (5) (2023) 611–613.

[17] Y. Yin, Y. Yin, X. Jiang, M.A. Koten, J.E. Shield, X. Chen, Y. Yun, A.T. N'Diaye, X. Hong, X. Xu, Spin rectification and electrically controlled spin transport in molecular-ferroelectrics-based spin valves, Phys. Rev. A 13 (6) (2023).

[18] Gavin David Scott, Douglas Natelson, Kondo resonances in molecular devices, ACS Nano 4 (7) (2010) 3560–3579.

[19] Riccardo Frisenda, Rocco Gaudenzi, Carlos Franco, Marta Mas-Torrent, Concepció Rovira, Jaume Veciana, Isaac Alcon, Stefan T. Bromley, Enrique Burzurí, Herre S.J. van der Zant, Kondo effect in a neutral and stable all organic radical single molecule break junction, Nano Lett. 15 (5) (2015) 3109–3114.

[20] Gerrit E.W. Bauer, Eiji Saitoh, Bart J. van Wees, Spin caloritronics, Nature Mater. 11 (2012) 391–399.

[21] Jianwei Li, Bin Wang, Fuming Xu, Yadong Wei, Jian Wang, Spin-dependent Seebeck effects in graphene-based molecular junctions, Phys. Rev. B 93 (19) (2016) 195426.

[22] Xiangnan Sun, Saül Vélez, Ainhoa Atxabal, Amilcar Bedoya-Pinto, Subir Parui, Xiangwei Zhu, Roger Llopis, Fèlix Casanova, Luis E. Hueso, A molecular spin-photovoltaic device, Science 357 (6352) (2017) 677–680.

[23] Y. Li, Q. Sun, The superior catalytic CO oxidation capacity of a Cr-phthalocyanine porous sheet, Sci. Rep. 4 (2023).

[24] Clément Barraud, Karim Bouzehouane, Cyrile Deranlot, Stéphane Fusil, Hashim Jabbar, Jacek Arabski, Rajib Rakshit, Dong-Jik Kim, Christophe Kieber, Samy Boukari, Martin Bowen, Eric Beaurepaire, Pierre Seneor, Richard Mattana, Frédéric Petroff, Unidirectional spin-dependent molecule-ferromagnet hybridized states anisotropy in cobalt phthalocyanine based magnetic tunnel junctions, Phys. Rev. Lett. 114 (20) (2015) 206603.

[25] A. Atxabal, M. Ribeiro, S. Parui, L. Urreta, E. Sagasta, X. Sun, R. Llopis, F. Casanova, L.E. Hueso, Spin doping using transition metal phthalocyanine molecules, Nature Commun. 7 (13751) (2016) 1–7.

[26] C. Barraud, K. Bouzehouane, C. Deranlot, D.J. Kim, R. Rakshit, S. Shi, J. Arabski, M. Bowen, E. Beaurepaire, S. Boukari, F. Petroff, P. Seneor, R. Mattana, Phthalocyanine based molecular spintronic devices, Dalton Trans. 45 (42) (2016) 16694–16699.

[27] Jing Huang, Ke Xu, Shulai Lei, Haibin Su, Shangfeng Yang, Qunxiang Li, Jinlong Yang, Iron-phthalocyanine molecular junction with high spin filter efficiency and negative differential resistance, J. Chem. Phys. 136 (6) (2012).

[28] Emilia Annese, Giovanni Di Santo, Fadi Choueikani, Edwige Otero, Philippe Ohresser, Iron phthalocyanine and ferromagnetic thin films:, ACS Omega 4 (3) (2019) 5076.

[29] R. Coldea, D.A. Tennant, E.M. Wheeler, E. Wawrzynska, D. Prabhakaran, M. Telling, K. Habicht, P. Smeibidl, K. Kiefer, Quantum criticality in an Ising chain: experimental evidence for emergent E8 symmetry, Science 327 (5962) (2010) 177–180.

[30] Sougato Bose, Quantum communication through spin chain dynamics: An introductory overview, Contemp. Phys. 48 (1) (2007) 13–30.

[31] Zhenlin Wu, Peter Robaschik, Luke R. Fleet, Solveig Felton, Gabriel Aeppli, Sandrine Heutz, Controlling ferromagnetic ground states and solitons in thin films and nanowires built from iron phthalocyanine chains, Adv. Funct. Mater. 29 (30) (2019) 1902550.

[32] Xike Wang, Hongbo Wang, Gang Chen, Magnetic properties of FePc sheet modified by the adsorption of gas molecules, Comput. Theor. Chem. 1214 (2022) 113793.

[33] S.X. Du Y.Y. Zhang, H.-J. Gao, Binding configuration, electronic structure, and magnetic properties of metal phthalocyanines on a Au (111) surface studied with ab initio calculations, Phys. Rev. B 84 (12) (2011).

[34] Juan Bartolomé, Fernando Bartolomé, Nicholas B. Brookes, Francesco Sedona, Andrea Basagni, Daniel Forrer, Mauro Sambi, Reversible fe magnetic moment switching in catalytic oxygen reduction reaction of Fe-phthalocyanine adsorbed on Ag(110), J. Phys. Chem. C 119 (22) (2015) 12488–12495.

[35] P. Schattschneider, S. Rubino, C. Hébert, Circular dichroism in the transmission electron microscope, in: Encyclopedia of Materials: Science and Technology, Elsevier, Walthm, MA, USA, 2007, pp. 1–11.

[36] Juan Bartolomé, Carlos Monton, Ivan K. Schuller, Magnetism of Metal Phthalocyanines, (no. 9783642406089) 2014.

[37] Huayan Xia, Lihong Li, Mei Fang, Tim S. Jones, Junliang Yang, Molecular-orientation-dependent magnetic properties of iron phthalocyanine (Fepc) thin films and microwires, 2023, [Online; Accessed 26 April 2023].

[38] H.C. Herper, S. Bhandary, O. Eriksson, B. Sanyal, B. Brena, Fe phthalocyanine on Co(001): Influence of surface oxidation on structural and electronic properties, Phys. Rev. B 89 (8) (2014) 085411.

[39] F. Petraki, H. Peisert, U. Aygül, F. Latteyer, J. Uihlein, A. Vollmer, T. Chassé, Electronic structure of FePc and interface properties on Ag(111) and Au(100), J. Phys. Chem. C 116 (20) (2012) 11110–11116.

[40] Ruoning Li, Na Li, Hao Wang, Alexander Weismann, Yajie Zhang, Shimin Hou, Kai Wu, Yongfeng Wang, Tuning the spin-related transport properties of FePc on Au(111) through single-molecule chemistry, Chem. Commun. 54 (66) (2018) 9135–9138.

[41] Marcin Roland Zemła, Kamil Czelej, Jacek A. Majewski, Graphene–Iron(II) phthalocyanine hybrid systems for scalable molecular spintronics, J. Phys. Chem. C 124 (50) (2020) 27645–27655.

[42] Soumyajyoti Haldar, Sumanta Bhandary, Hakkim Vovusha, Biplab Sanyal, Comparative study of electronic and magnetic properties of iron and cobalt phthalocyanine molecules physisorbed on two-dimensional MoS_2 and graphene, Phys. Rev. B 98 (8) (2018) 085440.

[43] Yu Wang, Xiaoguang Li, Jinlong Yang, Electronic and magnetic properties of CoPc and FePc molecules on graphene: The substrate, defect, and hydrogen adsorption effects, Phys. Chem. Chem. Phys. 21 (10) (2019) 5424–5434.

[44] Xiangru Kong, Hongkee Yoon, Myung Joon Han, Liangbo Liang, Switching interlayer magnetic order in bilayer CrI3 by stacking reversal, Nanoscale 13 (38) (2021) 16172–16181.

[45] Jihai Zhang, Yu Guo, Peigen Li, Jun Wang, Si Zhou, Jijun Zhao, Donghui Guo, Dingyong Zhong, Imaging vacancy defects in single-layer chromium triiodide, J. Phys. Chem. Lett. 12 (9) (2021) 2199–2205.

[46] Michele Pizzochero, Atomic-scale defects in the two-dimensional ferromagnet CrI3 from first principles, J. Phys. D: Appl. Phys. 53 (24) (2020) 244003.

[47] Rongrong Ma, Yun Sun, Mei Ge, Chenrui Ma, Junfeng Zhang, Electronic and magnetic properties of charged point defects in monolayer CrI3, Phys. Chem. Chem. Phys. 25 (12) (2023) 8809–8815.

[48] Batjargal Sainbileg, Erdembayalag Batsaikhan, Michitoshi Hayashi, Impact of oxygen defects on a ferromagnetic CrI 3 monolayer, RSC Adv. 10 (69) (2020) 42493–42501.

[49] Dongsi Wu, Ying Zhao, Yibin Yang, Le Huang, Ye Xiao, Shanshan Chen, Yu Zhao, Atomic intercalation induced spin-flip transition in bilayer CrI3, Nanomaterials 12 (9) (2022).

[50] Min Lu, Qiushi Yao, Qiongyu Li, Chuanyun Xiao, Chengxi Huang, Erjun Kan, Tuning electronic and magnetic properties of two-dimensional ferromagnetic semiconductor CrI3 through adsorption of benzene, J. Phys. Chem. C 124 (40) (2020) 22143–22149.

[51] Philip J. Hasnip, Keith Refson, Matt I.J. Probert, Jonathan R. Yates, Stewart J. Clark, Chris J. Pickard, Density functional theory in the solid state, Philos. Trans. R. Soc. A 372 (2011) (2014) 20130270.

[52] Paolo Giannozzi, Stefano Baroni, Nicola Bonini, Matteo Calandra, Roberto Car, Carlo Cavazzoni, Davide Ceresoli, Guido L. Chiarotti, Matteo Cococcioni, Ismaila Dabo, et al., QUANTUM ESPRESSO: A modular and open-source software project for quantum, J. Phys.: Condens. Matter. 21 (39) (2009) 395502.

[53] John P. Perdew, Kieron Burke, Matthias Ernzerhof, Generalized gradient approximation made simple, Phys. Rev. Lett. 77 (18) (1996) 3865–3868.

[54] Shamik Chakraborty, Abhilash Ravikumar, Substrate induced electronic phase transitions of CrI_3 based van der Waals heterostructures, Sci. Rep. 11 (198) (2021) 1–12.

[55] Matteo Cococcioni, Stefano de Gironcoli, Linear response approach to the calculation of the effective interaction parameters in the LDA + U method, Phys. Rev. B 71 (3) (2005) 035105.

[56] Iulia Emilia Brumboiu, Soumyajyoti Haldar, Johann Lüder, Olle Eriksson, Heike C. Herper, Barbara Brena, Biplab Sanyal, Influence of electron correlation on the electronic structure and magnetism of transition-metal phthalocyanines, J. Chem. Theory Comput. 12 (4) (2016) 1772–1785.

[57] Jiayong Zhang, Bao Zhao, Tong Zhou, Yang Xue, Chunlan Ma, Zhongqin Yang, Strong magnetization and Chern insulators in compressed graphene/CrI_3 van der Waals heterostructures, Phys. Rev. B 97 (8) (2018) 085401.

[58] Z.H. Cheng, L. Gao, Z.T. Deng, N. Jiang, Q. Liu, D.X. Shi, S.X. Du, H.M. Guo, H.-J. Gao, Adsorption behavior of iron phthalocyanine on Au(111) surface at submonolayer coverage, J. Phys. Chem. C 111 (26) (2007) 9240–9244.

[59] Stefan Grimme, Semiempirical GGA-type density functional constructed with a long-range dispersion correction, J. Comput. Chem. 27 (15) (2006) 1787–1799.

[60] Matyáš Novák, Jiří Vackář, Robert Cimrman, Evaluating Hellmann–Feynman forces within non-local pseudopotentials, Comput. Phys. Comm. 250 (2020) 107034.

[61] Hendrik J. Monkhorst, James D. Pack, Special points for Brillouin-zone integrations, Phys. Rev. B 13 (12) (1976) 5188–5192.

[62] Jianhua Chen, Zhenghe Xu, Ye Chen, Electronic structure and surfaces of sulfide minerals, Elsevier, Walthm, MA, USA, 2020,

[63] George Bruhn, Ernest R. Davidson, Istvan Mayer, Aurora E. Clark, Löwdin population analysis with and without rotational invariance, Int. J. Quantum Chem. 106 (9) (2006) 2065–2072.

[64] Z.H. Cheng, L. Gao, Z.T. Deng, N. Jiang, H.-J. Gao, Adsorption behavior of iron phthalocyanine on Au(111) surface at submonolayer coverage, J. Phys. Chem. C - J PHYS CHEM C 111 (26) (2007).

[65] Nils Richter, Daniel Weber, Franziska Martin, Nirpendra Singh, Udo Schwingenschlögl, Bettina V. Lotsch, Mathias Kläui, Temperature-dependent magnetic anisotropy in the layered magnetic semiconductors CrI_3 and $CrBr_3$, Phys. Rev. Mater. 2 (2) (2018) 024004.

[66] Lucas Webster, Liangbo Liang, Jia-An Yan, Distinct spin–lattice and spin–phonon interactions in monolayer magnetic CrI3, Phys. Chem. Chem. Phys. 20 (36) (2018) 23546–23555.

[67] Javier Polanco-Gonzalez, Jesús Alfredo Carranco-Rodríguez, José L. Enríquez-Carrejo, Pierre G. Mani-Gonzalez, José Manuel Domínguez-Esquivel, Manuel Ramos, Band gap tuning in 2D layered materials by angular rotation, Materials 10 (2) (2017) 147.

[68] Artem V. Kuklin, Maxim A. Visotin, Woohyeon Baek, Paul V. Avramov, CrI3 magnetic nanotubes: A comparative DFT and DFT+U study, and strain effect, Physica E 123 (2020) 114205.

[69] Haiyang Pan, Xiaobo Wang, Qiaoming Wang, Xiaohua Wu, Chang Liu, Nian Lin, Yue Zhao, Proximity Effect of epitaxial iron phthalocyanine molecules on high-quality graphene devices, Chin. Phys. Lett. 38 (8) (2021) 087201.

[70] Bevin Huang, Genevieve Clark, Efrén Navarro-Moratalla, Dahlia R. Klein, Ran Cheng, Kyle L. Seyler, Ding Zhong, Emma Schmidgall, Michael A. McGuire, David H. Cobden, et al., Layer-dependent ferromagnetism in a van der Waals crystal down to the monolayer limit, Nature 546 (7657) (2017) 270–273.

[71] Shengwei Jiang, Lizhong Li, Zefang Wang, Kin Fai Mak, Jie Shan, Controlling magnetism in 2D CrI 3 by electrostatic doping, Nat. Nanotechnol. 13 (7) (2018) 549–553.

[72] Heiko Peisert, Johannes Uihlein, Fotini Petraki, Thomas Chassé, Charge transfer between transition metal phthalocyanines and metal substrates: The role of the transition metal, J. Electron Spectrosc. Relat. Phenom. 204 (2015) 49–60.

[73] Y.Y. Zhang, S.X. Du, H.-J. Gao, Binding configuration, electronic structure, and magnetic properties of metal phthalocyanines on a Au(111) surface studied with ab initio calculations, Phys. Rev. B 84 (12) (2011) 125446.

[74] Sumanta Bhandary, Saurabh Ghosh, Heike Herper, Heiko Wende, Olle Eriksson, Biplab Sanyal, Graphene as a reversible spin manipulator of molecular magnets, Phys. Rev. Lett. 107 (25) (2011) 257202.

[75] Liwei Liu, Kai Yang, Yuhang Jiang, Boqun Song, Wende Xiao, Linfei Li, Haitao Zhou, Yeliang Wang, Shixuan Du, Min Ouyang, Werner A. Hofer, Antonio H. Castro Neto, Hong-Jun Gao, Reversible single spin control of individual magnetic molecule by hydrogen atom adsorption, Sci. Rep. 3 (1210) (2013) 1–5.

[76] Christian Wäckerlin, Dorota Chylarecka, Armin Kleibert, Kathrin Müller, Cristian Iacovita, Frithjof Nolting, Thomas A. Jung, Nirmalya Ballav, Controlling spins in adsorbed molecules by a chemical switch, Nature Commun. 1 (61) (2010) 1–7.

[77] Jun Hu, Ruqian Wu, Control of the magnetism and magnetic anisotropy of a single-molecule magnet with an electric field, Phys. Rev. Lett. 110 (9) (2013) 097202.

[78] Zhen Liu, Yongzheng Guo, Zhiyong Chen, Tao Gong, Yue Li, Yuting Niu, Yingchun Cheng, Haipeng Lu, Longjiang Deng, Bo Peng, Observation of intrinsic crystal phase in bare few-layer CrI3, Nanophotonics 11 (19) (2022) 4409–4417.

[79] Sakthipandi Kathiresan, Manu Selvam, Phase transition of La0.62Sr0.38MnO3 perovskite manganites, ResearchGate 1 (2019) 28–30.

[80] J. Krishnamurthy, A. Venimadhav, Magnetic field-induced metamagnetic, magnetocaloric and pyrocurrent behaviors of Eu2CoMnO6, J. Magn. Magn. Mater. 500 (2020) 166387.

[81] T. Murata, H. Kushida, T. Terai, T. Kakeshita, Pressure-induced magnetic transition of layered manganite La2-2xSr1+2xMn2O7 (x=0.315, 0.318), J. Magn. Magn. Mater. 310 (2, Part 2) (2007) 1555–1557.

[82] Eric Collet, Nicolas Moisan, Chérif Baldé, Roman Bertoni, Elzbieta Trzop, Claire Laulhé, Maciej Lorenc, Marina Servol, Hervé Cailleau, Antoine Tissot, Marie-Laure Boillot, Timothy Graber, Robert Henning, Philip Coppens, Marylise Buron-Le Cointe, Ultrafast spin-state photoswitching in a crystal and slower consecutive processes investigated by femtosecond optical spectroscopy and picosecond X-ray diffraction, Phys. Chem. Chem. Phys. 14 (18) (2012) 6192–6199.

[83] Jian Zhou, Qian Wang, Qiang Sun, Yoshiyuki Kawazoe, Puru Jena, Strain-induced spin crossover in phthalocyanine-based organometallic sheets, J. Phys. Chem. Lett. 3 (21) (2012) 3109–3114.

[84] Peter Dowben, Half metallic ferromagnets, J. Phys.: Condens. Matter. 19 (31) (2007) 310301.

[85] Yilv Guo, Shijun Yuan, Bing Wang, Li Shi, Jinlan Wang, Half-metallicity and enhanced ferromagnetism in Li-adsorbed ultrathin chromium triiodide, J. Mater. Chem. C 6 (21) (2018) 5716–5720.

[86] M. Seredyuk, A.B. Gaspar, V. Ksenofontov, Y. Galyametdinov, M. Verdaguer, F. Villain, P. Gütlich, One-dimensional iron(II) compounds exhibiting spin crossover and liquid crystalline properties in the Room Temperature Region, Inorg. Chem. 47 (22) (2008) 10232–10245.

[87] Iulia Cojocariu, Dr. Silvia Carlotto, Henning Maximilian Sturmeit, Dr. Giovanni Zamborlini, Prof. Mirko Cinchetti, Dr. Albano Cossaro, Dr. Alberto Verdini, Dr. Luca Floreano, Dr. Matteo Jugovac, Prof. Peter Puschnig, Dr. Cinthia Piamonteze, Prof. Maurizio Casarin, Dr. Vitaliy Feyer, Prof. Claus Michael Schneider, Ferrous to ferric transition in Fe-Phthalocyanine driven by NO2 exposure, Chemistry (Weinheim an Der Bergstrasse, Germany) 27 (10) (2021) 3526.